Supporting Information

Complete reconstruction of NiMoO$_4$/NiFe LDH for enhanced oxygen evolution reaction

Shuya Zhang,[a] Mingjun Cen,[a] Qianqiao Wang,[a] Xinyu Luo,[a] Wenchao Peng,[a] Yang Li,[a]

Fengbao Zhang,[a] and Xiaobin Fan*[a,b,c]

[a] School of Chemical Engineering and Technology, State Key Laboratory of Chemical

Engineering, Tianjin University, Tianjin, 300354, China.

[b] Haihe Laboratory of Sustainable Chemical Transformations, Tianjin 300192, China

[c] Institute of Shaoxing, Tianjin University, Zhejiang 312300, China

[*] Corresponding authors.

E-mail addresses: xiaobinfan@tju.edu.cn

Experimental section

Materials. Ammonium molybdate tetrahydrate [$(NH_4)_6Mo_7O_{24}.4H_2O$, 99%, Aladdin], nickel nitrate hexahydrate [$Ni(NO_3)_2.6H_2O$, 98%, Aladdin], ferrous sulfate heptahydrate ($FeSO_4.7H_2O$, AR, Heowns), and urea [$CO(NH_2)_2$, 99%, Aladdin]. Deionized water was used to prepare all the aqueous solutions. All these chemicals were utilized without further purification.

Synthesis of hierarchical NiMoO₄/NiFe LDH. Firstly, $NiMoO_4$ nanorods were grown on nickel foam by hydrothermal method. 0.992g ammonium molybdate tetrahydrate [$(NH_4)_6Mo_7O_{24}.4H_2O$] and 0.928g nickel nitrate hexahydrate [$Ni(NO_3)_2.6H_2O$] were dissolved in 50 mL deionized water under stirring to form a homogeneous solution. The above solution and a piece of pretreated NF (3 cm × 5 cm) were transferred to a 100 mL Teflon-lined autoclave, sealed, and kept at 150 °C for 6 h. Then, the obtain $NiMoO_4$ nanorods were immersed into a mixed solution of nickel nitrate (0.24g), ferrous sulfate (0.08g), urea (0.32g) and kept at 80°C for 30h to construct hierarchical $NiMoO_4$/NiFe LDH ($NiMoO_4$/NiFe LDH Fe-25%) pre-catalysts. $NiMoO_4$/NiFe LDH (Fe-x%, x=50, 70, and 90) was prepared by changing the content of Fe in the mixed solution.

Synthesis of NiMoO₄. $NiMoO_4$ nanorods were grown on nickel foam by hydrothermal. 0.992g ammonium molybdate tetrahydrate [$(NH_4)_6Mo_7O_{24}.4H_2O$] and 0.928g nickel nitrate hexahydrate [$Ni(NO_3)_2.6H_2O$] were dissolved in 50 mL deionized water under stirring to form a homogeneous solution. The above solution and a piece of pretreated NF (3 cm × 5 cm) were transferred to a 100 mL Teflon-lined autoclave, sealed, and kept at 150 °C for 6 h.

Synthesis of NiFe LDH. A piece of pretreated NF (3 cm × 5 cm) was immersed into a mixed solution of nickel nitrate (0.24g) and ferrous sulfate (0.08g), urea (0.32g) and kept at 80°C for 30h. Then, the as-prepared sample was washed with deionized water.

Characterizations. The morphologies of samples were characterized by field scanning electron microscopy (SEM, S4800, HITACHI). High-resolution electron transmission images and energy dispersive spectroscopy (EDS) were obtained by a JEM-F200

Microscope. The crystal structure of samples was detected by an X-ray diffraction spectrometer (XDR, Bruker AXS D8 Focus). The chemical composition was detected by inductive couple plasma-optical spectroscopy (ICP-OES, Thermo ICAP PRO) and X-ray photoelectron spectroscope (XPS, Thermo Fischer, ESCALAB 250Xi). In-situ Raman measurements were performed on a confocal microscopic system (LabRAM HR Evolution, Horiba, France) equipped with a semiconductor laser (λ = 532 nm, Laser Quantum Ltd.). The Raman spectra were collected continuously with a step of 0.05 or 0.1 mV during chronoamperometry measurement.

Electrochemical measurements. All the electrochemical measurements were performed on CHI-760E with a standard three-electrode system in 1M KOH. The prepared catalyst-loaded nickel foams (NF) were directly utilized as the working electrode. The reference electrode and counter electrode were Ag/AgCl electrode using saturated KCl solution as salt bridging, and carbon rod, respectively. All potentials were converted into reversible hydrogen electrode values (vs. RHE) according to the equation: $E_{RHE}=E_{Ag/AgCl}+0.197+0.059\times pH$. Before recording, the working electrode was scanned for 50 cycles at the scan rate of 50 mV/s without *IR* compensation in 1.0 M KOH solution. Linear sweep voltammetry (LSV) was performed to evaluate OER activity at a scan rate of 1.0 mV/s. Electrochemical impedance spectra (EIS) were obtained in the range of 0.1 Hz-100 kHz with an amplitude of 5 mV at 1.51V. The electrochemically active surface was estimated by measuring the double-layer capacitance (C_{dl}) in the non-faradaic region at different scan rates with cyclic voltammetry. The selected potential window and scan rate ranges were 0.9-1.0 V and 20-120mV/s, respectively. The long-term stability of catalysts was evaluated by chronopotentiometry measurement.

TOF calculation. The turnover frequency (TOF) of the pre-active site is based on the following equations:

$$n = \frac{Q}{4F}$$
(1)

Where n is the number of active sites estimated in pH=7 phosphate buffer at a scan rate of 50 mV/s, Q is the number of voltametric charges calculated by integrating CV

curves, and F is the Faraday constant (96485 C mol^{-1}).

$$TOF = \frac{j * A}{4 * F * n} \qquad (2)$$

Where j is current density, A is the geometric area of the working electrode. Note that the physical unit of j*A is ampere.

FE calculation. The faraday efficiency was calculation by the following equation:

$$FE = \frac{V_{exp.}}{V_{the.}} = \frac{V_{exp.}}{\dfrac{V_m Q}{4F}} \qquad (3)$$

Where $V_{exp.}$ is the measured volume of generated O_2 (mL), $V_{the.}$ is the theoretical volume of O_2 (mL), Q is the electric charges (C), V_m is the molar volume of gas (24.5 L/mol), and full-cell water splitting was performed in an H-type cell with a proton exchange membrane.

DFT calculation. In this work, DFT calculations were performed by Vienna Ab initio Simulation Package (VASP) with the projector augmented wave (PAW) method. The exchange-related function utilized was Perdew-Burke-Ernzerhof (PBE). The cut-off energy specified by ENCUT was set to 500 eV for cell optimization and calculation of the electronic structure. The modeling was performed with a vacuum spacing of at least 15 Å in the direction of the vertical catalyst surface to prevent interference. Taking into account the large structural model, the Brillouin zone integration was performed using 5 × 5 × 1 Monkhorst-Pack k-point sampling for primitive cells. To improve the calculation accuracy, the value of parameter EDIFF was set to 10^{-5} eV. The relaxation was stopped when the norms of all the forces are smaller than 0.02 eV/Å.
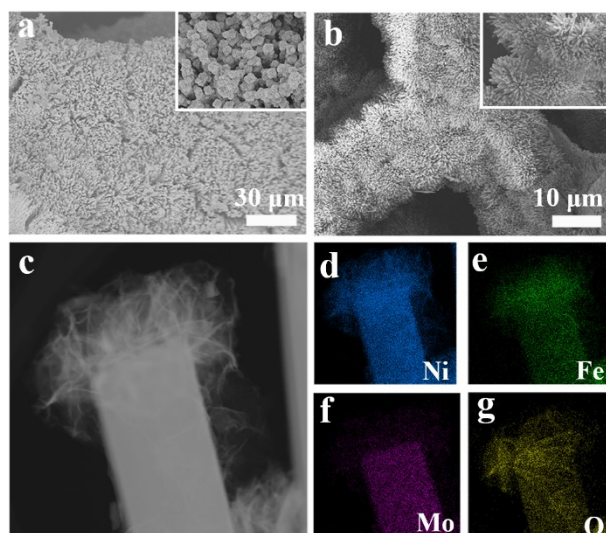
Fig. S1. (a) SEM image of $NiMoO_4$/NiFe LDH. (b) SEM images of $NiMoO_4$. (c) TEM image of $NiMoO_4$/NiFe LDH. (d)-(g) EDS mapping of $NiMoO_4$/NiFe LDH.
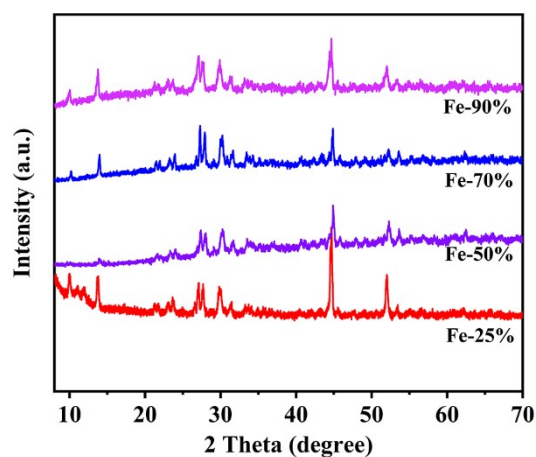

Fig. S2. XRD patterns of $NiMoO_4$/NiFe LDH with different Fe content.

The XRD patterns of hybridized $NiMoO_4$/NiFe LDH with different Fe content show that the variable content of Fe influences the crystal structure of $Ni(OH)_2$, but has a negligible influence on the structure of $NiMoO_4$. Note that $NiMoO_4$/NiFe LDH (Fe-25%) has a better crystal structure.
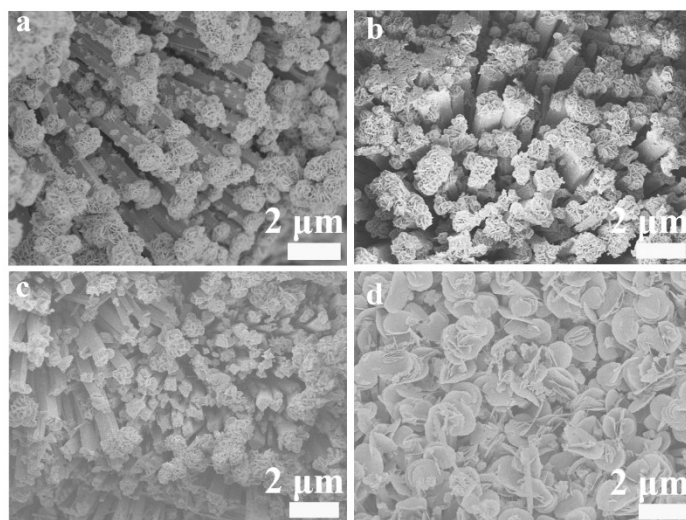
Fig. S3. SEM images of NiMoO$_4$/NiFe LDH with different Fe content. (a) Fe-25%. (b)Fe-50%. (c) Fe-70%. (d) Fe-90%.

The SEM images of hybridized NiMoO$_4$/NiFe LDH with different Fe content show that the content of Fe has a significant influence on the hierarchical structure of catalysts. We find that NiMoO$_4$/NiFe LDH (Fe-25%) exhibits a better hierarchical structure than other samples.
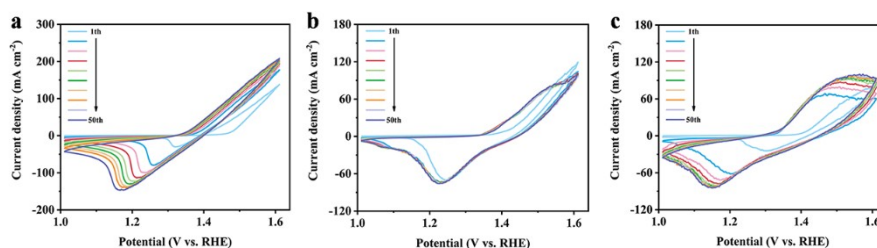

Fig. S4. The evolution of CV curves at the scan of 50 mV/s. (a) NiMoO$_4$/NiFe LDH. (b) NiFe LDH. (c) NiMoO$_4$.
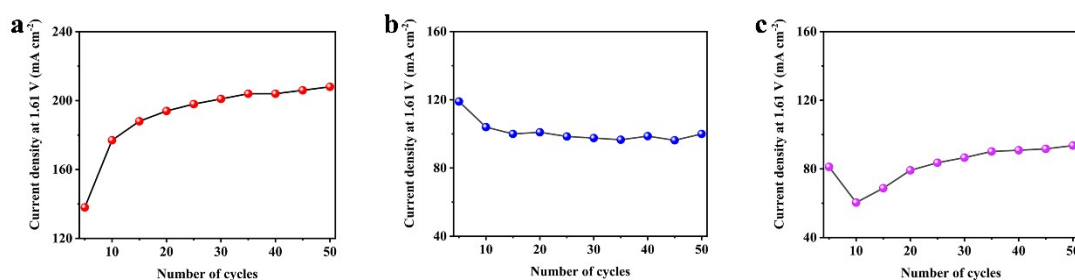

Fig. S5. The cut-off current density at 1.61 V vs. RHE. (a) NiMoO$_4$/NiFe LDH. (b) NiFe LDH. (c) NiMoO$_4$.
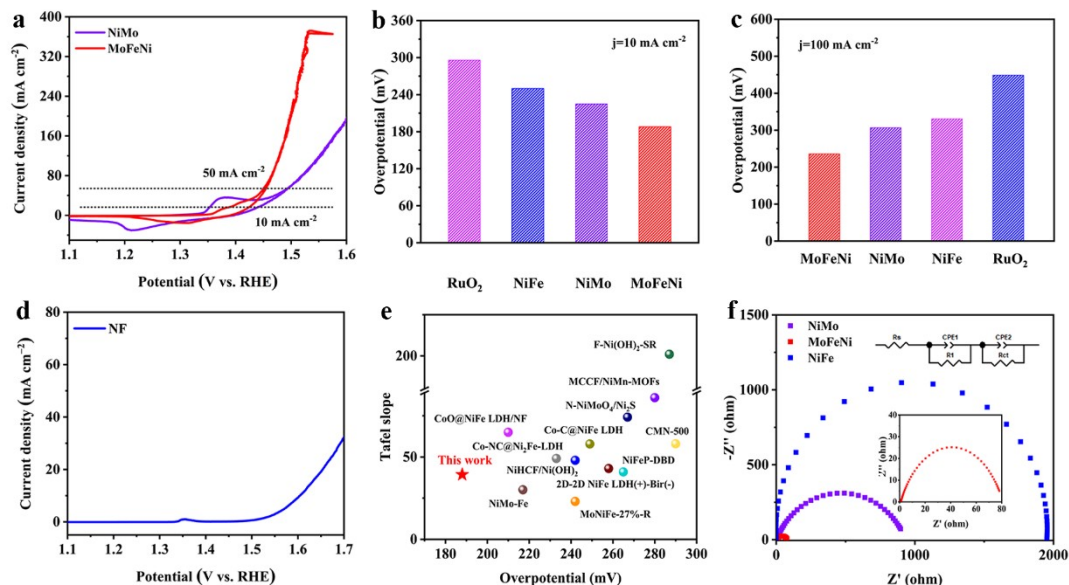
Fig. S6. (a) Cyclic voltammetry polarization curves. (b) and (c) Overpotentials at 10 and 100 mA cm⁻², respectively. (d) LSV curve for NF. (e) Comparison of overpotentials and Tafel slopes at 10 mA cm^{-2} for currently reported transition metal OER electrocatalysts. (f) Electrochemical impedance spectra of MoFeNi, NiFe, and NiMo.
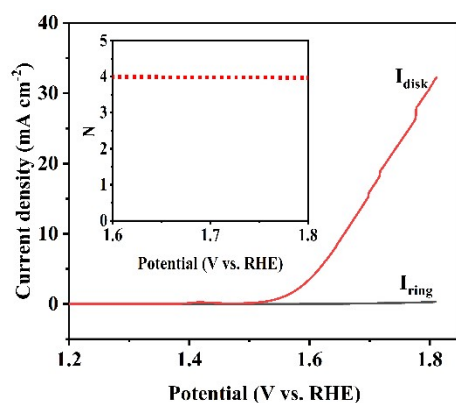

Fig. S7. RRDE voltammogram and the calculated N for MoFeNi.

As shown in Fig. S7, the ring current (I_{ring}) is negligible in the 1.6-1.8 V range compared to the disk current (I_{disk}). Moreover, the average electron numbers calculated from RRDE measurement show that experimental OER is consistent with the theoretical 4-electron process.
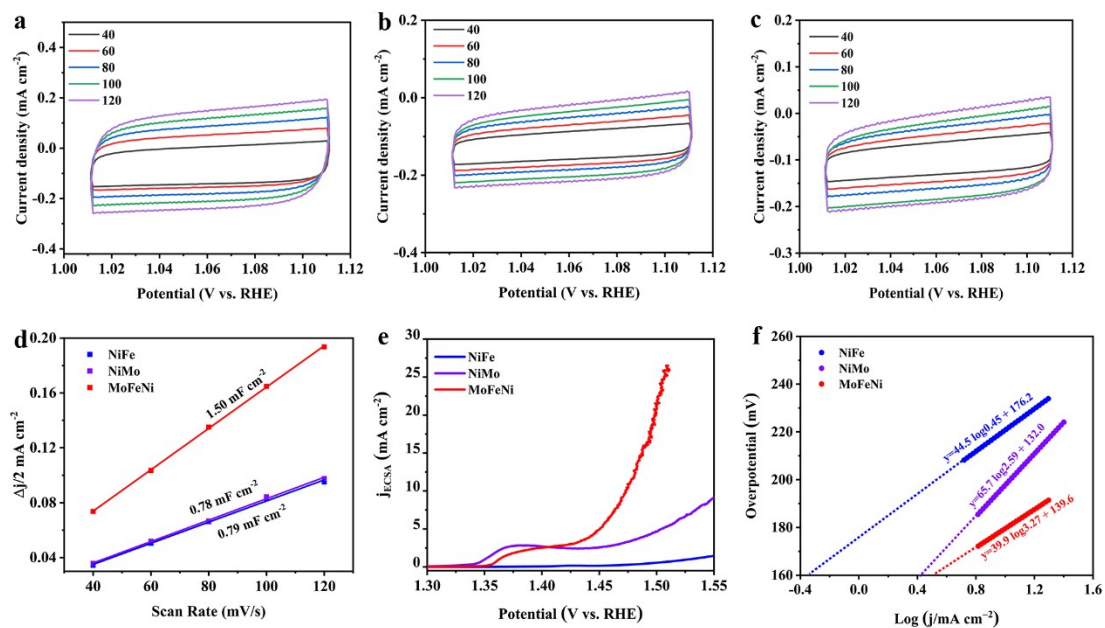
Fig. S8. (a), (b), and (c) CV curves at different scan rates of MoFeNi, NiMo, and NiFe, respectively. (d) Current density versus scan rate profiles for estimating C_{dl}. (e) Current density normalized by ECSA. (f) Exchange current density of NiFe, NiMo, and MoFeNi.
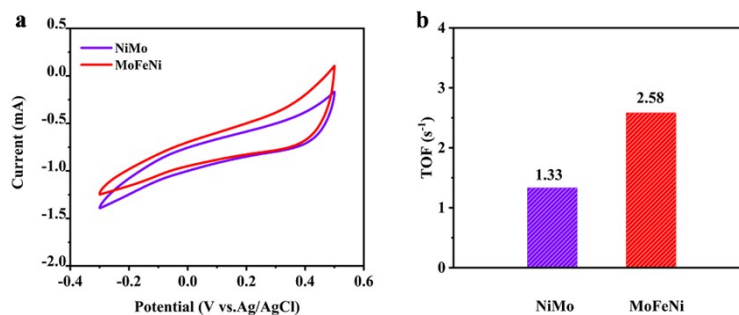

Fig. S9. (a) CV curves of NiMo and MoFeNi in pH=7 phosphate buffer. (b) Turnover frequencies of catalysts at the overpotential of 280 mV in 1.0 M KOH.
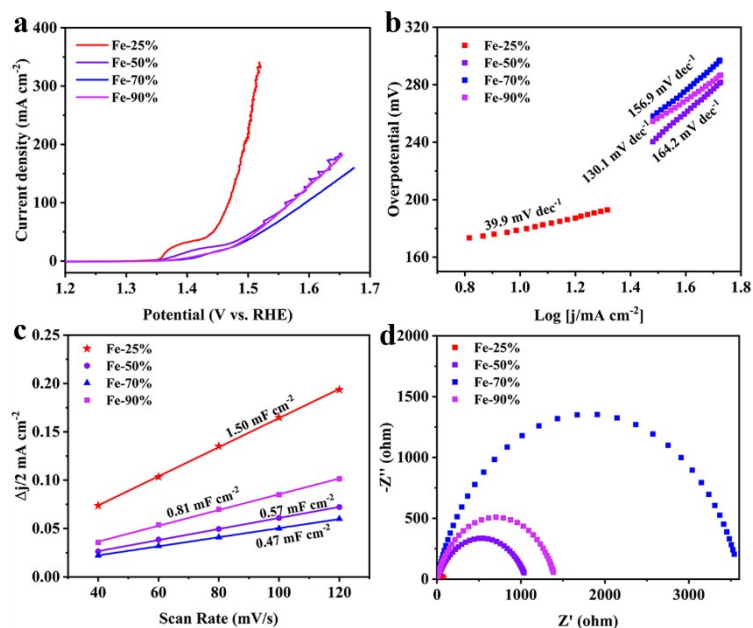
Fig. S10. OER performance for NiMoO$_4$/NiFe LDH with different Fe content. (a) LSV curves. (b) Tafel plots. (c) Current density versus scan rate profiles for estimating C_{dl}. (d) EIS curves.

We evaluated the OER performance of NiMoO$_4$/NiFe LDH with different Fe content after complete reconstruction. As shown in Fig. S10a and b, NiMoO$_4$/NiFe LDH(Fe-25%) exhibits the lowest overpotential and Tafel slope, suggesting better OER activity and faster electrochemical kinetic. Furthermore, NiMoO$_4$/NiFe LDH(Fe-25%) holds more ECSA and a faster charge transfer rate, which may be attributed to a well-hierarchical structure and effective adjustment of electronic structure (Fig. S10c and d). Therefore, NiMoO$_4$/NiFe LDH (Fe-25%) is selected for analyzing complete reconstruction behavior.
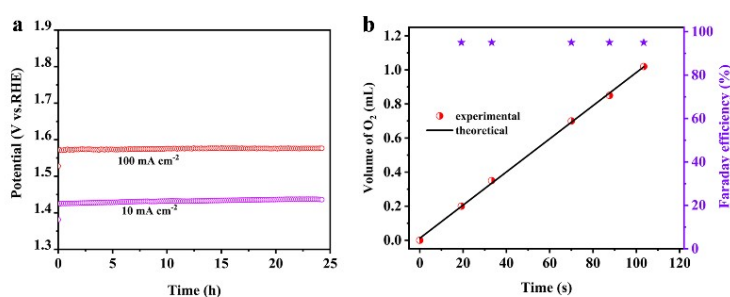

Fig. S11. (a) Chronopotentiometry curves at the current density of 10 and 100 mA cm^{-2}. (b) Experimental and theoretical volumes of O$_2$ and Faraday efficiency.
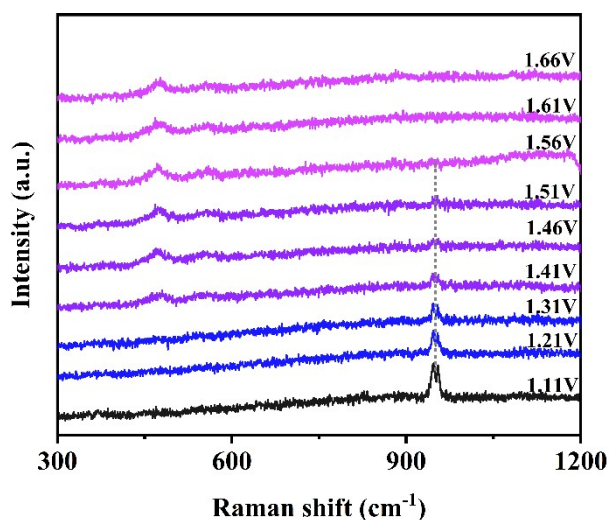
Fig. S12. *In-situ* Raman spectra of NiMoO$_4$.

As shown in Fig. S12, Mo–O vibration at 948 cm^{-1} disappears until the anode potential reached 1.56 V, which is higher than that of NiMoO$_4$/NiFe LDH. This result suggests that NiMoO$_4$/NiFe LDH is more favorable for the selective etching of MoO$_4^{2-}$ and achieving faster phase transformation during complete reconstruction.
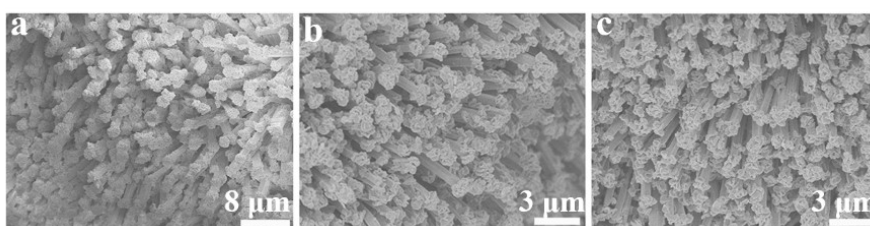

Fig. S13. SEM images of NiMoO$_4$/NiFe LDH that underwent the *in-situ* Raman process. (a) 1.11 V. (b) 1.51 V. (c) 1.66 V.
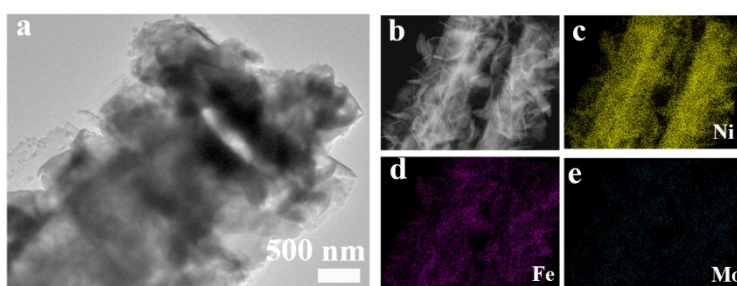

Fig. S14. (a) Low magnification TEM of MoFeNi. (b)-(e) EDS mapping of MoFeNi.
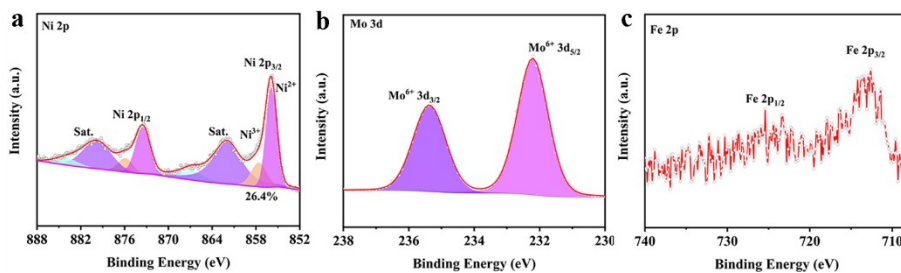
Fig. S15. XPS spectra of NiMoO$_4$/NiFe-LDH pre-catalyst (a) Ni 2p. (b) Mo 3d. (c) Fe 2p.

As shown in Fig. S15a, the peaks located at 855.9 eV and 857.6 eV are attributed to Ni^{2+} 2p$_{3/2}$ and Ni^{3+} 2p$_{3/2}$ in NiMoO$_4$/NiFe-LDH pre-catalyst, respectively. [1,2] The content of Ni^{3+} species in NiMoO$_4$/NiFe-LDH pre-catalyst before reconstruction is calculated to be 26.4%. The high-resolution XPS of Mo 3d is shown in Fig. 15b. The two peaks at 232.2 eV and 235.4 eV are ascribed to Mo^{6+} 3d$_{5/2}$ and Mo^{6+} 3d$_{3/2}$, respectively.[3] Besides, the Fe 2p XPS is displayed in Fig. 15c. The peak at 713.3 eV is derived from Fe^{3+} 2p$_{3/2}$ in NiMoO$_4$/NiFe-LDH pre-catalyst.[4] The XPS results of the NiMoO$_4$/NiFe-LDH pre-catalyst suggest that the oxidative states of Ni, Mo, and Fe species are mainly Ni^{2+}, Mo^{6+}, and Fe^{3+}, respectively.
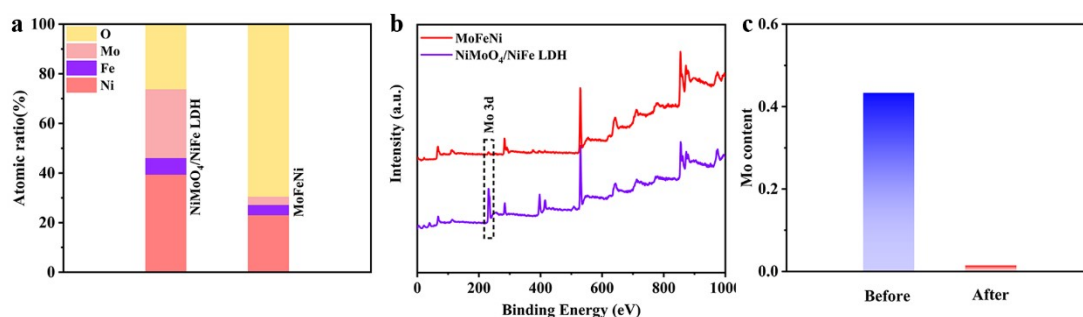

Fig. S16. (a) Element composition changes of samples before and after reconstruction measured by EDS. (b) XPS spectra of NiMoO$_4$/NiFe LDH before and after reconstruction. (c). Mo content in the sample before and after reconstruction.
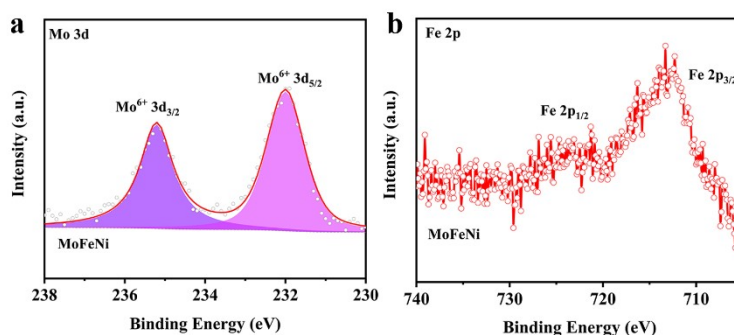

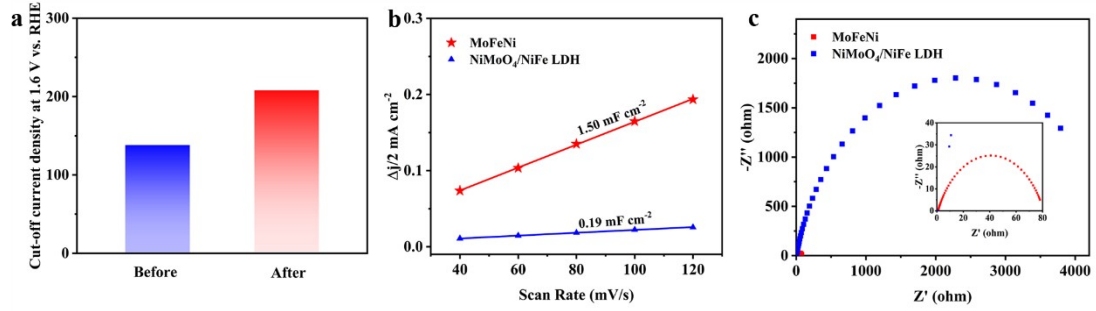**Fig. S17.** XPS spectra for MoFeNi. (a) Mo 3d. (b). Fe 2p.

Fig. S18. Electrochemical tests of NiMoO$_4$/NiFe LDH before and after complete reconstruction. (a) cut-off current density. (b) Current density versus scan rate profiles for estimating C_{dl}. (c) EIS curves.

To further demonstrate the positive effect of complete reconstruction, we analyzed the electrochemical data before and after reconstruction. As shown in Fig. S18a, the cut-off current density increases from 138 to 208 mA cm^{-2} at 1.6 V (without IR compensation). Afterward, the C_{dl} value before and after complete reconstruction is calculated to be 0.19 and 1.50 mF cm^{-2}, indicating that the sample has a larger ECSA after reconstruction (Fig. S18b). Besides, the sample after reconstruction has the smallest R_{ct} value, suggesting reconstruction facilitates the faster charge transfer (Fig. S18c). These results elucidate that the complete reconstruction has a positive effect on the OER process of NiMoO$_4$/NiFe LDH pre-catalyst.
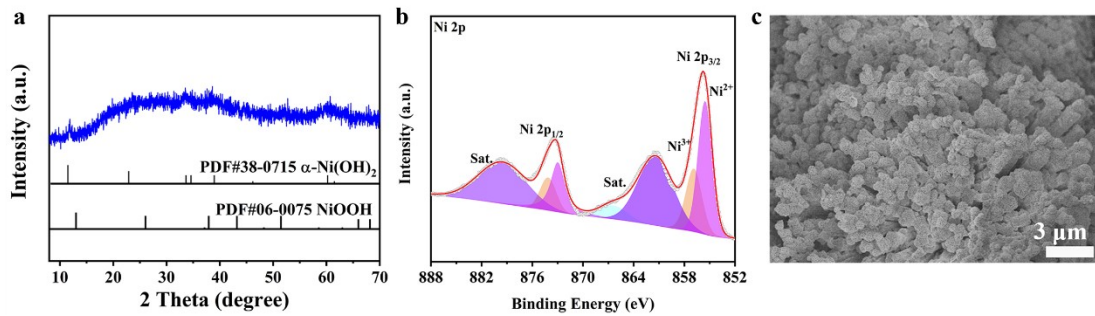

Fig. S19. The structural and morphological characterization of MoFeNi after 48 h OER. (a) XRD pattern. (b). Ni 2p XPS. (c) SEM image.

As shown in Fig. S19, we characterized the structure and morphology of MoFeNi after 48 h OER. The XRD pattern shows that Ni(OH)$_2$ and NiOOH phases can be well preserved (Fig. S19a). This result is consistent with the presence of abundant Ni^{3+} (Fig. S19b). Besides, the SEM image of MoFeNi after 48 h OER is shown in Fig. S19c and hierarchical morphology can be observed. These results indicate MoFeNi possesses pretty structural and morphological stability.
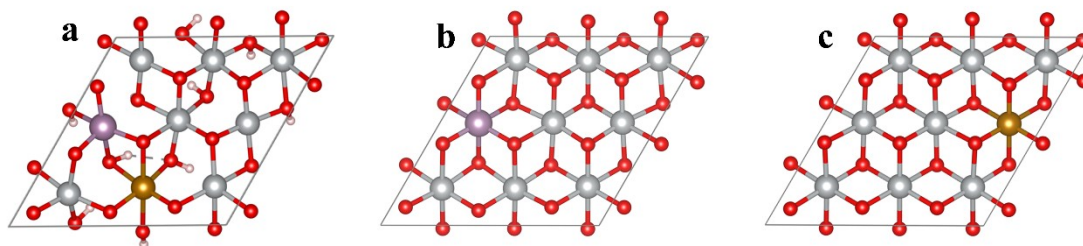
Figure S20. Structure models for DFT calculations. (a) MoFeNi. (b) NiMo. (c) NiFe.
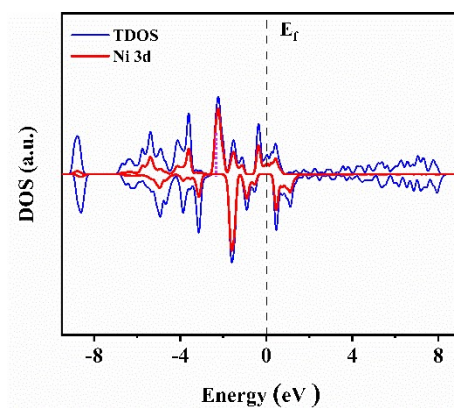

Fig. S21. The density of states (DOS) and d-band center level of Ni 3d orbitals in NiOOH.
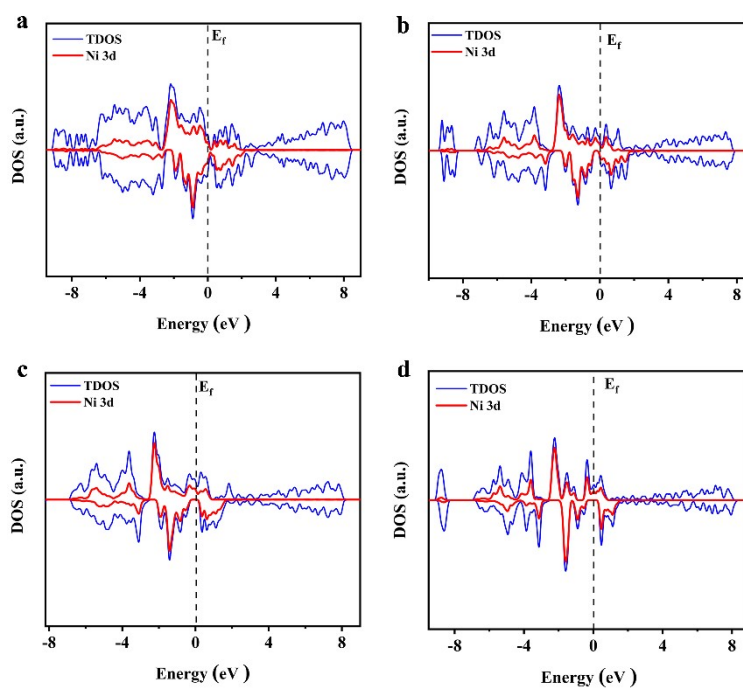

Fig. S22. The total density of state (TDOS, blue) and projected density of state (PDOS, red) of Ni 3d orbitals for MoFeNi, NiMo, and NiFe.

Table S1. The overpotential and Tafel slope comparison between our work and other reported Ni-based electrocatalysts.

electrocatalysts	electrolyte	Overpotential (mV) at 10 mA cm^{-2}	Tafel slop	Ref.
MoFe -Ni (oxy)hydroxide	1.0 M KOH	188	39.9	This work
CMN-500	1.0 M KOH	290	58.0	[5]
F-Ni(OH)$_2$-SR	1.0 M KOH	287	201	[6]
MCCF/NiMn-MOFs	1.0 M KOH	280	86	[7]
NiHCF/Ni(OH)$_2$	1.0 M KOH	242	48	[8]
MoNiFe-27%-R	1.0 M KOH	242	23	[9]
NiFeCoLDH/CF	1.0 M KOH	249	42	[10]
NiFeP-DBD	1.0 M KOH	265	40.9	[11]
NiMo-Fe	1.0 M KOH	217	30.1	[3]
Co-C@NiFe LDH	1.0 M KOH	249	57.9	[12]
NiFe-MoOx NS	1.0 M KOH	276	56.0	[13]
2D-2D NiFe LDH(+)-Bir(-)	1.0 M KOH	258	43	[14]
CoO@NiFe LDH/NF	1.0 M KOH	210	65	[15]
S-NiFe (oxy)hydroxide/CNT	1.0 M KOH	190	\	[16]
N-NiMoO$_4$/NiS$_2$	1.0 M KOH	267	74.2	[17]
Co-NC@Ni$_2$Fe-LDH	1.0 M KOH	233	49.1	[18]
Ni(Fe)OOH-Fe$_2$O$_3$	1.0 M KOH	230	41	[19]

Table S2. The overpotentials at 50 mA cm^{-2} for different catalysts.

catalysts	MoFeNi	NiMo	NiFe
Overpotential (mV) at 50 mA cm^{-2}	210	258	289

Table S3. The metal content in the KOH electrolyte.

elements	Mo	Fe	Ni
loading amount (µg/L)	789917.9	28.2	457.4

Table S4. The d-band center level for Ni 3d orbitals of different structures.

Structures	MoFeNi	NiMo	NiFe	NiOOH
d-band center level (eV)	−2.07	−2.60	−2.35	−2.37

References

1 J. Lv, L. Wang, R. Li, K. Zhang, D. Zhao, Y. Li, X. Li, X. Huang and G. Wang, *ACS Catal.*, 2021, **11**, 14338-14351.

2 N. Zhang, X. Feng, D. Rao, X. Deng, L. Cai, B. Qiu, R. Long, Y. Xiong, Y. Lu and Y. Chai, *Nat. Commun.*, 2020, **11**, 4066.

3 H. Liao, X. Zhang, S. Niu, P. Tan, K. Chen, Y. Liu, G. Wang, M. Liu and J. Pan, *Appl. Catal. B: Environ.*, 2022, **307**, 121150.

4 J. Ge, J. Y. Zheng, J. Zhang, S. Jiang, L. Zhang, H. Wan, L. Wang, W. Ma, Z. Zhou and R. Ma, *J. Mater. Chem. A*, 2021, **9**, 14432-14443.

5 J. Bai, J. Mei, T. Liao, Q. Sun, Z. G. Chen and Z. Sun, *Adv. Energy Mater.*, 2021, **12**, 2103247.

6 Y. Kang, S. Wang, K. S. Hui, S. Wu, D. A. Dinh, X. Fan, F. Bin, F. Chen, J. Geng, W.-C. M. Cheong and K. N. Hui, *Nano Res.*, 2021, **15**, 2952-2960.

7 W. Cheng, X. F. Lu, D. Luan and X. W. Lou, 2022, **59**, 18234–18239.

8 W. Hua, H. Sun, M. Jiang, L. Ren, Y. Zhang and J.-G. Wang, *J. Mater. Chem. A*, 2022, **10**, 7366-7372.

9 Z. He, J. Zhang, Z. Gong, H. Lei, D. Zhou, N. Zhang, W. Mai, S. Zhao and Y. Chen, *Nat. Commun.*, 2022, **13**, 2191.

10 Y. Lin, H. Wang, C. K. Peng, L. Bu, C. L. Chiang, K. Tian, Y. Zhao, J. Zhao, Y. G. Lin, J. M. Lee and L. Gao, *Small*, 2020, **16**, 2002426.

11 T. Wang, X.-Z. Fu and S. Wang, *Green Energy Environ.*, 2022, **7**, 365-371.

12 W. Li, S. Chen, M. Zhong, C. Wang and X. Lu, *Chem. Eng. J.*, 2021, **415**, 128879.

13 C. Xie, Y. Wang, K. Hu, L. Tao, X. Huang, J. Huo and S. Wang, *J. Mater. Chem. A*, 2017, **5**, 87-91.

14 X. Long, Z. Chen, M. Ju, M. Sun, L. Jin, R. Cai, Z. Wang, L. Dong, L. Peng, B. Huang and S. Yang, *Angew. Chem. Int. Ed.*, 2021, **60**, 9699-9705.

15 Z. Wang, J. Zhang, Q. Yu, H. Yang, X. Chen, X. Yuan, K. Huang and X. Xiong, *Chem. Eng. J.*, 2021, **410**, 128366.

16 T. Wang, G. Nam, Y. Jin, X. Wang, P. Ren, M. G. Kim, J. Liang, X. Wen, H. Jang, J. Han, Y. Huang, Q. Li and J. Cho, *Adv. Mater.*, 2018, **30**, 1800757.

17 L. An, J. Feng, Y. Zhang, R. Wang, H. Liu, G.-C. Wang, F. Cheng and P. Xi, *Adv. Funct. Mater.*, 2019, **29**, 1805298.

18 T. Guo, L. Chen, Y. Li and K. Shen, *Small*, 2022, **18**, 2107739.

19 H. Yang, C. Dong, H. Wang, R. Qi, L. Gong, Y. Lu, C. He, S. Chen, B. You, H. Liu, J. Yao, X. Jiang, X. Guo and B. Y. Xia, *Proc. Natl. Acad. Sci. U. S. A.*, 2022, **119**, 2202812119.